LS-DYNA® 980 : Recent Developments, Application Areas and Validation Process of the Incompressible fluid solver (ICFD) in LS-DYNA

Part 2

Iñaki Çaldichoury
Facundo Del Pin

Livermore Software Technology Corporation
7374 Las Positas Road
Livermore, CA 94551

Abstract

LS-DYNA version 980 will include CFD solvers for both compressible and incompressible flows. The solvers may run as standalone CFD solvers where only fluid dynamics effects are studied or they could be coupled to the solid mechanics and thermal solvers of LS-DYNA to take full advantage of their capabilities in order to solve fluid-structure interaction (FSI) problems.

This paper will focus on the Incompressible CFD solver in LS-DYNA (ICFD) and will be divided in two parts. Part one will present some advanced features of the solver as well some recent developments or improvements. Part two will provide some insight on the validation process that is currently under way in order to better understand the present capabilities and state of advancement of the solvers. Several test cases and results will be presented that will highlight several main features and potential industrial application domains of the solvers. The future steps and the challenges that remain will also be discussed.

1- Typical applications of the ICFD solver

The first application that generally comes to one's mind when referring to a fluid mechanics (CFD) solver is to study the drag around vehicles. This type of problems can be classified as "External aerodynamics" problems. In fluid mechanics, an external flow is such a flow that boundary layers develop freely, without constraints imposed by adjacent surfaces. Accordingly, there will always exist a region of the flow outside the boundary layer in which velocity, temperature, and/or concentration gradients are negligible. It can be defined as the flow of a fluid around a body that is completely submerged in it. External flow test cases have so far focused on bluff bodies. A bluff body is one in which the length in the flow direction is close to or equal to the length perpendicular to the flow direction which usually results in a skin friction drag that is much lower than the pressure drag.

Another classic application would be "Internal aerodynamics" flows that include flows in pipes, ducts, air conducts, cavities, jet engines or wind tunnels. In fluid mechanics, an internal flow is a flow for which the fluid is constrained by a surface. Hence the boundary layer is unable to develop without eventually being constrained. The internal flow configuration represents a convenient geometry for heating and cooling fluids used in chemical processing, environmental control, and energy conversion technologies.

One of the solver's main features is to solve free surface problems. This opens a whole new array of applications that may involve waves, sloshing phenomena, interaction between ship hulls and water or, structural resistance of offshore petrol station pillars to wave impacts. Analyzes involving free surface can further be divided in two sub categories: slamming type analyzes (bodies entering or impacting the fluid) or moving waves analyzes (incoming wave impacting a structure).

The incompressible fluid solver's coupling with the solid mechanics solver can be done using either loose coupling or strong coupling. Loose coupling is usually sufficient for aerodynamic problems where the solid density is several orders of magnitude higher than the fluids and where the structure usually does not deform too much. However, for such applications where the density of the fluid is close to the solids (blood vessels, rubber materials) or when the time step is too small, a so-called added mass effect occurs which bring instabilities that require a strong coupling between the fluid and the solid as well as the development of special stabilization techniques [1]. Several industrial application type models have already been built with the ICFD solver giving satisfactory qualitative result, the next step currently under investigation will be to validate the FSI features in critical cases where the added mass effect is significant.

Lastly, the ICFD solver also includes the solving of the heat equation in the fluid allowing conjugate heat transfer analyzes. Potential applications are numerous and include refrigeration, air conditioning, building heating, motor coolants, defrost or even heat transfer in the human body. Furthermore, the ICFD thermal solver is fully coupled with the structural thermal solver using a monolithic approach which allows solving complex problems where both heated structures and flows are present and interact together. Validation test cases for this feature will also be provided in the future.

2- External Aerodynamics

2-1 The flow around a cylinder

2-1-1 Model Description

The flow behind a circular cylinder has always been a major research and validation test case both for its simple geometry and for its great practical importance in engineering applications. This test case focuses on the steady laminar flow at low Reynolds numbers as well as on the unsteady vortex shedding, also called Von Karman Vortex Street, that appears with increasing Reynolds number (See Figure 1). Figure 2 offers a view of the mesh used. Based on a cylinder radius of unity, the surface element size of the cylinder will be 0.01. Several elements are added to the boundary layer in order to be able to accurately calculate the friction drag.
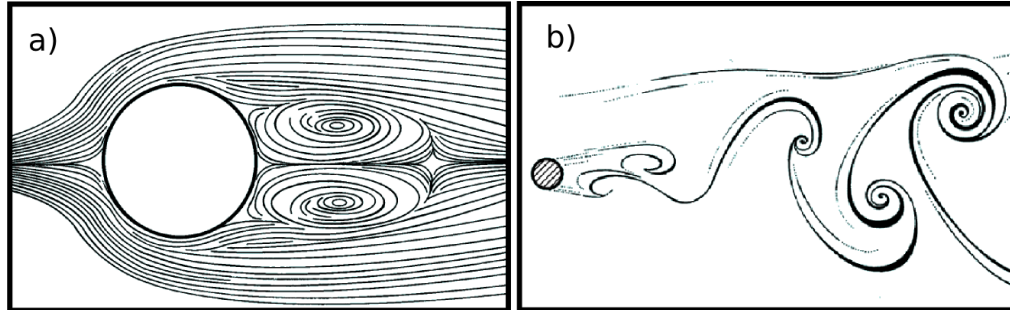
Figure 1 a) Re=40, Symmetric flow separation b) Re=100, Von Karman Vortex Street
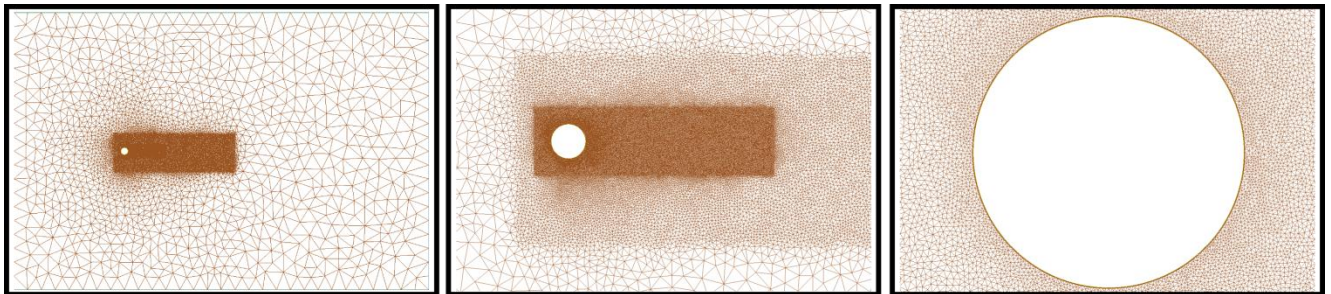

Figure 2 Various zooming levels on the mesh around the cylinder

2-1-2 Results

Figure 3 shows the velocity vectors for a Reynolds number of 40 highlighting the steady laminar symmetric separation occurring behind the cylinder as well as the velocity vectors for a Reynolds number of 100 with the periodic Von Karman vortex shedding. Figure 4 offers a comparison between the present analysis and the reference numerical results given by [2]. The lift values correspond to the maximum lift values occurring during the vortex shedding. Starting from the Reynolds value of 60, the drag values given are mean drag values calculated after the vortex shedding is fully developed. The global behavior of the present analysis is in good agreement with the reference results. Starting from the Reynolds number of 40, the error regarding the total drag slowly expands going from 3.8% for Re = 40 to 7.5% for Re = 2 when compared to the results given by [2]. This can be explained by the fact that, as the Reynolds number decreases and the viscosity increases, the hypothesis used by the Fractional Step method of the solver, (i.e the diffusion term of the solution due to the viscosity is small compared to the convection term) is progressively reaching its limits. It can also be noted that the error regarding the lift coefficient slowly increases going from 4.1% for Re = 80 to 6.6% for Re = 160. In order to bring this error down, a finer mesh may be used. For illustration purposes, Table 1 offers a mesh grid convergence analysis for a Reynolds number of 100 with the error calculation based on the reference result by [2].

Finally, for the Reynolds numbers of 40 and 100, some further observations can be made. For the Reynolds number of 40, the boundary layer separation angle occurs at an angle of 54° and the distance between the flow reattachment point and the cylinder is equal to 2.3 which is in very good agreement with the results given by [2]. For the Reynolds number of 100, the Strouhal number is equal to 0.165 which is in the vicinity of the results given by [2] and [3].
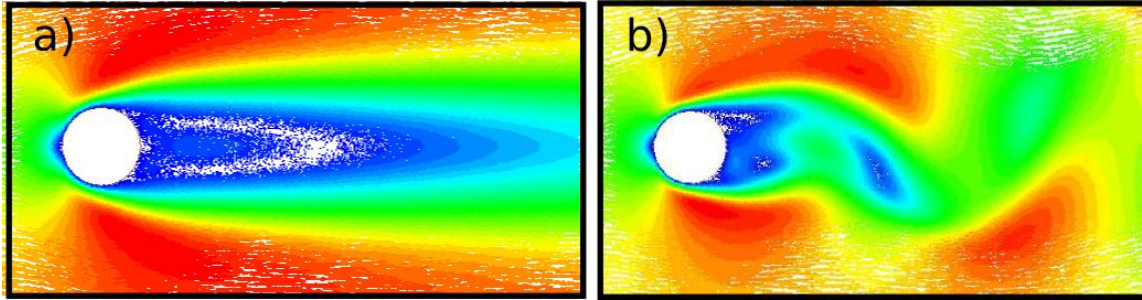
Figure 3 a) Re=40 Fluid Velocity Vectors, b) Re=100 Fluid Velocity Vectors

Cylinder Surface Element size	Cl_{tot}	Error
0.02	0.357	7.6%
0.01	0.346	4.2%
0.005	0.337	1.4%
0.0025	0.336	1.2%

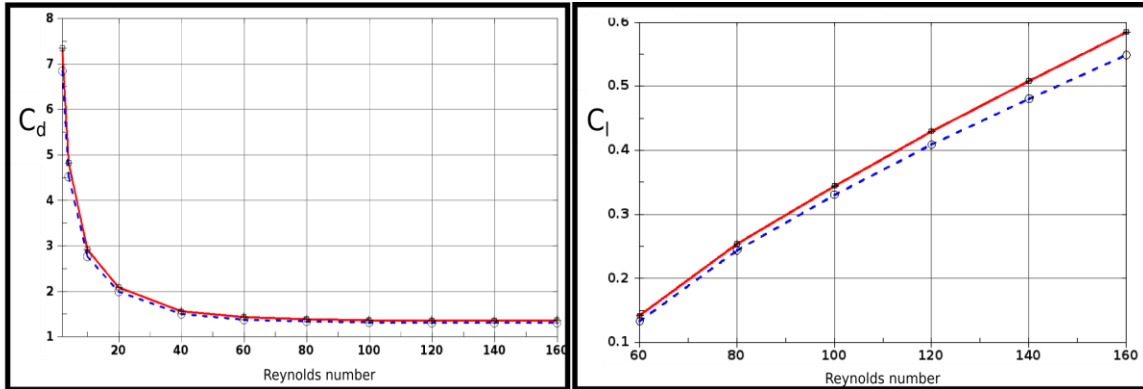**Table 1 Mesh grid analysis for Re=100 based on reference result by [2].**

Figure 4 Comparison between numerical results (in Red) and reference results by [2] (in Blue) for the Drag and Lift coefficients function of the Reynolds number.

2-2 The Ahmed body

2-2-1 Model Description

The Ahmed body is a very simplified geometry with no accessories or wheels. It is frequently employed as a benchmark in vehicle aerodynamics since it retains most of the primary behavior of the vehicle aerodynamics. A sketch of the body geometry is represented in Figure 5 where $L = 1044\,[mm]$, $B = 389\,[mm]$ and $H = 288\,[mm]$. Figure 5 also shows the behavior of the drag coefficient [4] based on the projected area $A = 389 \times 288\,[mm]^2$ function of the various slant angles $\alpha°$ with the following division:

- C_w the total drag coefficient of the body,
- C_r^* the total friction drag coefficient of the body,
- C_p^* the total pressure drag coefficient of the body,
- C_k^* the pressure drag coefficient of the front part of the body,
- C_b^* the pressure drag coefficient of the back part of the body,
- C_s^* the pressure drag coefficient of the slant part of the body.

Each of these drag components retain specific flow features and must therefore be studied separately. Accordingly, as can be seen on Figure 6, finer mesh zones will be defined closer to the front, slant and back parts of the body and some elements will be added in the anisotropic direction of the boundary layer in order to better capture the friction drag. The total number of elements for this case is approximately 7 million (mainly due to the fine mesh on the slant) with a surface mesh size of approximately 2 $[mm]$ on the slant and 6 $[mm]$ on the rest of the body. The incoming velocity will be chosen as $60\ m.s^{-1}$ resulting in a body length based Reynolds number of approximately $4.5e^6$. For this paper, the analysis will focus on the $12.5°$ slant angle case which corresponds to the critical point of lowest drag value. The Smagorinsky LES turbulence model available in the ICFD solver will be used.
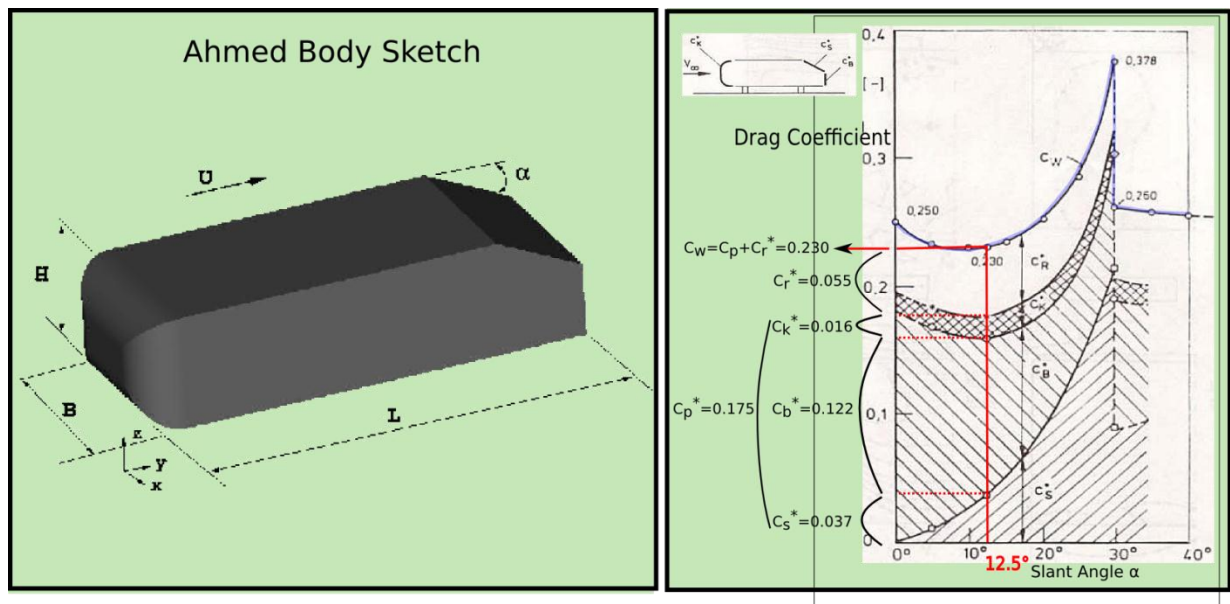

Figure 5 Ahmed body sketch and experimental drag coefficient results function of the slant angle α by [4]. Focus on the 12.5° slant angle.
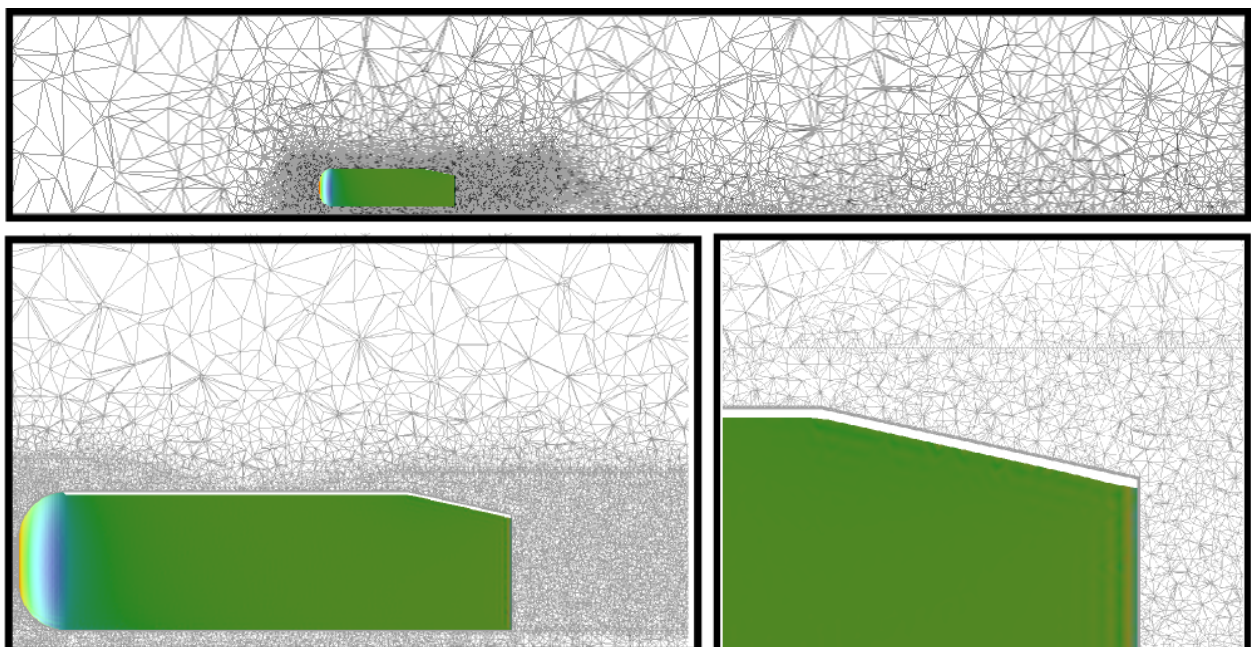

Figure 6 Various zoom levels on the mesh in the (x-z) plane.

5

2-2-2 Results

Figure 7 focuses on the front part and shows the surface pressure repartition of the body as well as the iso-contours of pressure in the (x-z) plane. It can be observed that the main contribution to the pressure drag C_k^* comes from the central face while depression zones or "bubbles" appear on the curved surfaces that lower the drag value. This explains the relatively low contribution of the front part to the total drag compared to the other parts of the body. The iso-contours of pressure in the cut-plane also show the blockage influence due to the proximity of the ground which causes a small dissymmetry in the pressure repartition on the front and results in a smaller suction bubble on the bottom curved surface.

Figure 8 shows the velocity fringes and streamlines over the body in the (x-z) plane. The flow remains attached over the slant and only separates when reaching the back part. This explains the low drag value of the slant C_s^* and the overall low value of the total drag C_w. Figure 9 offers a better visualization of the vortexes and recirculation areas forming in the wake of the body. Two side vortexes appearing at the tip of the slant are also captured and can be directly compared to the experimental results by [5].

Finally, the main contribution to the friction drag comes from the middle part of the body that entirely lies orthogonally to the incoming flow with minor contributions from the front and slant parts. Table 2 offers a comparison between the experimental results by [4] and the numerical results for the different parts and shows a globally good agreement.
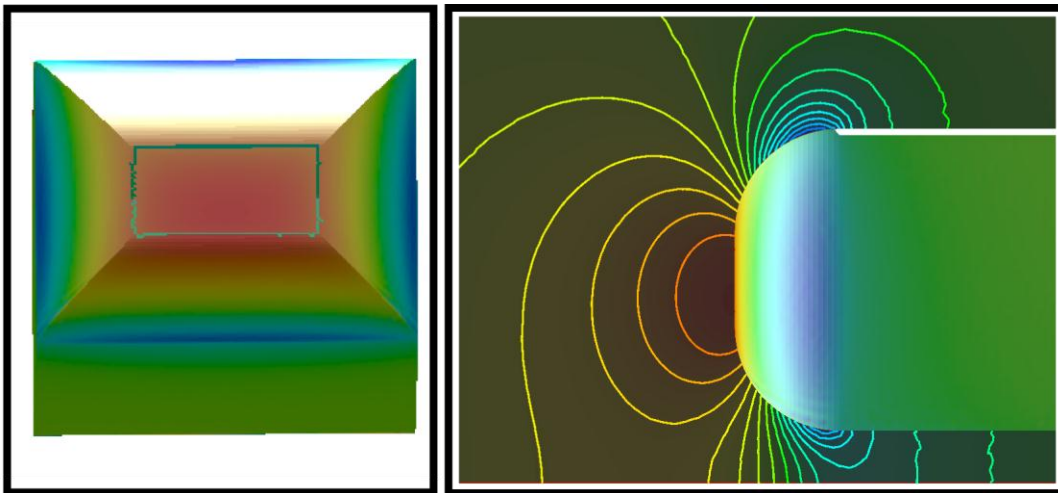

Figure 7 Surface pressure repartition on the front part of the body and pressure is-contours in the (x-z) plane
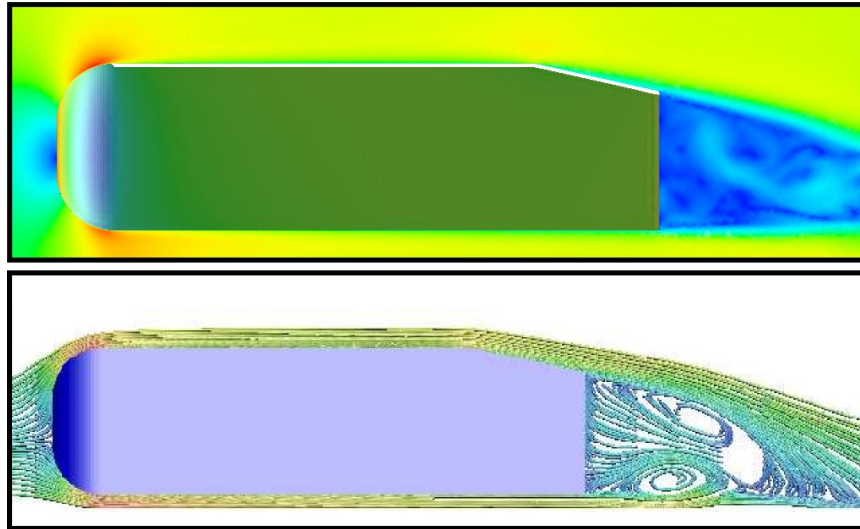
Figure 8 Velocity fringes and Streamlines in the (x-z) plane

Figure 9 Q criterion visualization in the wake of the body next to a picture from the experiment by [5]

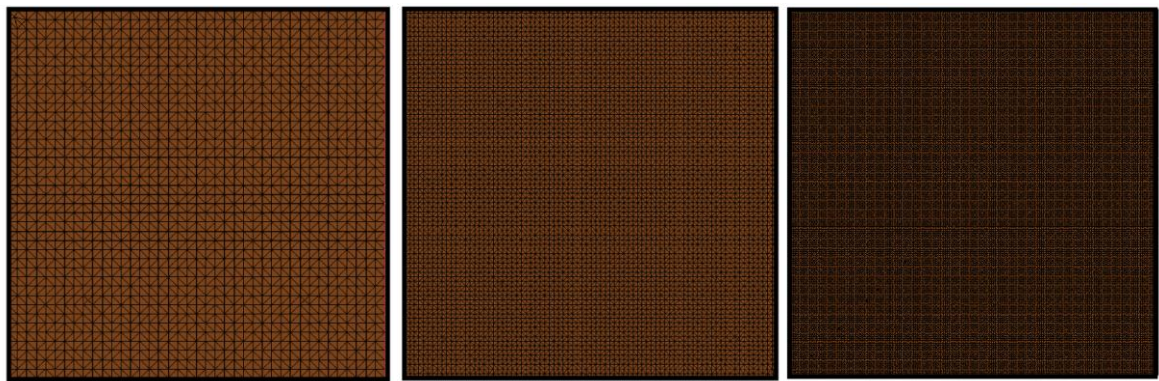|	Results by Ahmed & al. [4]	Numerical results	Error
C_s^*	0.037	0.040	8%
C_b^*	0.122	0.121	-1%
C_k^*	0.016	0.009	-43%
C_p^*	0.175	0.170	-2.8%
C_r^*	0.055	0.063	14%
C_w	0.230	0.233	1.3%

Table 2 Experimental and Numerical Results comparison for the 12.5° slant angle case

3- Internal Aerodynamics

3-1 The Cavity

3-1-1 Model Description

The driven cavity problem has long been used as a benchmarking test case for incompressible CFD solvers. The standard case is a fluid contained in a square domain with three stationary sides and one moving side (with velocity tangent to the side). Depending on the Reynolds number, different vortexes can appear at various locations. Several mesh sizes have been tried in order to offer a mesh convergence analysis (See Figure 10).

Figure 10 Cavity problem, different mesh sizes used

3-1-2 Results

Figure 11 shows the velocity fringes after the different cases have run. The main vortex can be clearly identified. The position of the vortexes is given for the finest meshes for every Reynolds number in Table 3. The results agree well with the reference results of [6], [7] and [8]. Figure 12 gives the velocity profiles along the x and y axis, using the center of the cavity as origin and highlights the convergence of the results with the mesh size.
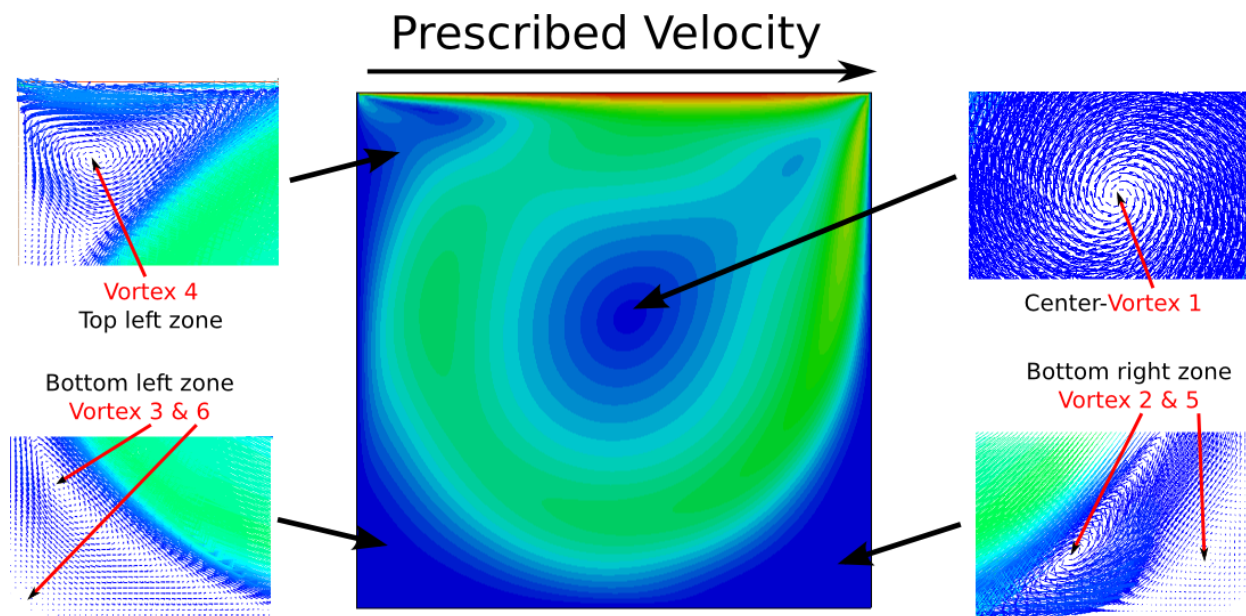

Figure 11 Velocity fringes and velocity vectors close to the vortexes' locations

Reynolds	Vortex 1	Vortex 2	Vortex 3	Vortex 4	Vortex 5	Vortex 6
1000	0.5313/0.5656	0.8625/0.1125	0.0844/0.0781			
5000	0.5156/0.5344	0.8030/0.0750	0.0750/0.1359	0.0656/0.9094	0.9813/0.0188	0.0045/0.0045
10 000	0.5125/0.5313	0.7656/0.5938	0.0563/0.1563	0.0688/0.9125	0.9313/0.0563	0.0125/0.0125

Table 3 Numerical results for vortexes positions ((x,y) coordinates) for the finer mesh case (160*160 elements)
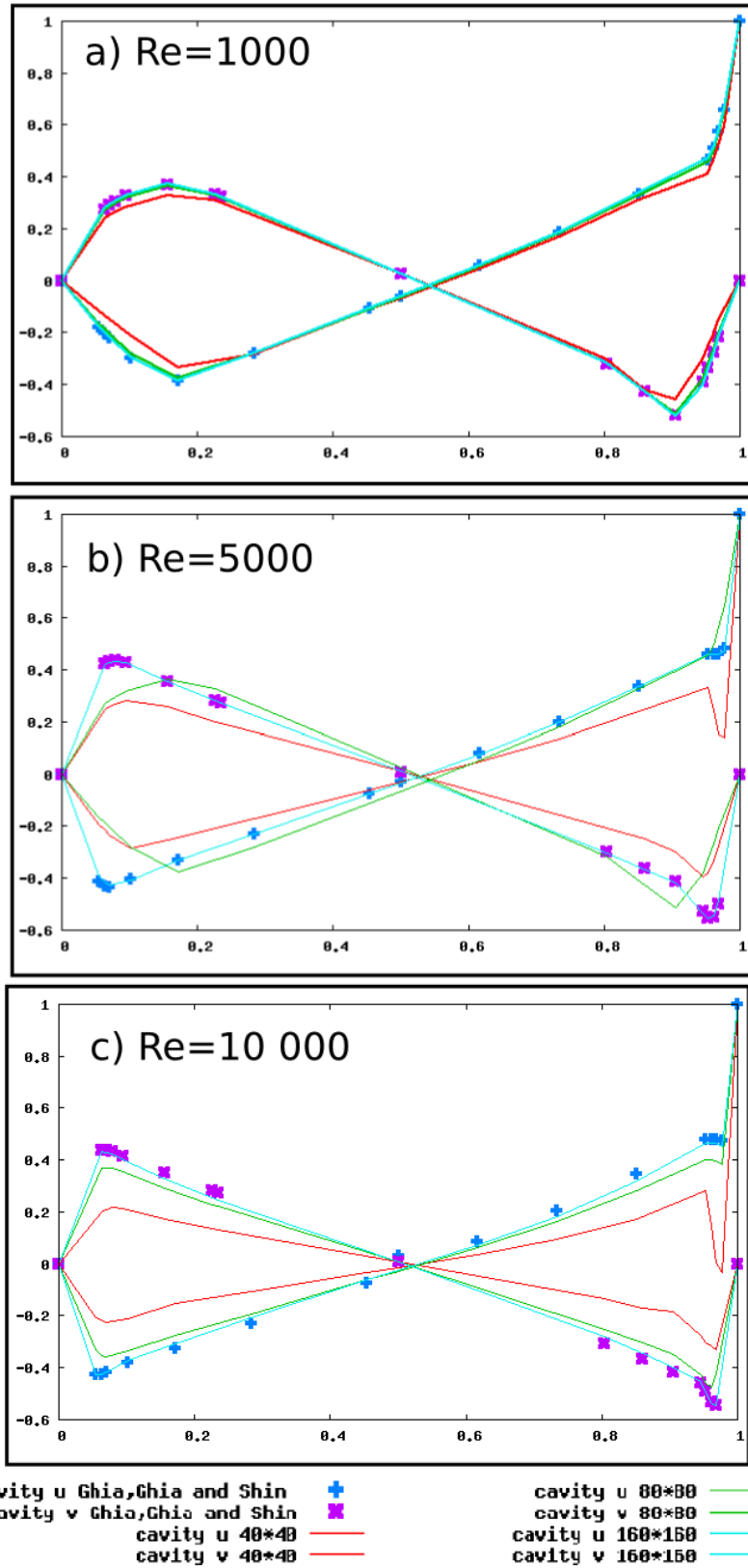
Figure 12 Cavity test case. Velocity profiles $U_x(x = 0.5)$ and $U_y (y = 0.5)$ for different mesh sizes and Reynolds numbers. Comparison with reference numerical results (points) by [6].

3-2 The Backward facing step

3-2-1 Model Description

The backward facing step is a challenging numerical problem based on a simple geometry but retaining rich flow physics. It consists of a duct flow with the channel suddenly expanding and creating one or several recirculation zones on the upper and lower parts of the channels depending on the Reynolds number (See Figure 13). As the Reynolds number grows, a finer mesh was used close to the recirculating zones in order to capture their location with more precision. Table (3) gives the mesh sizes used for the different Reynolds numbers.
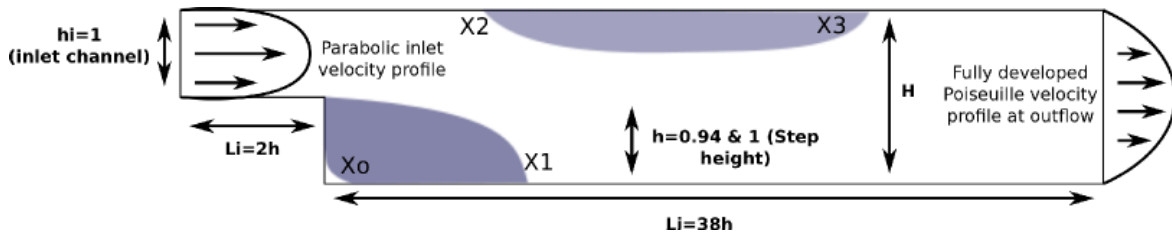

Figure 13 Sketch of the Backward-facing step. Position of the different recirculation zones

Reynolds	Mesh size used close to recirculation regions
0-400	0.05
500-700	0.025
700-1200	0.0125

Table 4 Mesh sizes used around the recirculation regions based on an inlet channel height equal to unity for the different Reynolds numbers.

3-2-2 Results

For these results, we choose to present the case with an expansion ratio ER of 2 i.e the outlet channel height is twice as big as the inlet channel. The results can be compared to the reference experimental results of [9] and to some reference numerical results of [10]. Figure 14 shows the coherent behavior compared to the experience as well as the excellent agreement with the reference numerical results. Small change in slopes can be observed for mesh size transitions with finer meshes resulting in closer agreements to the reference results.
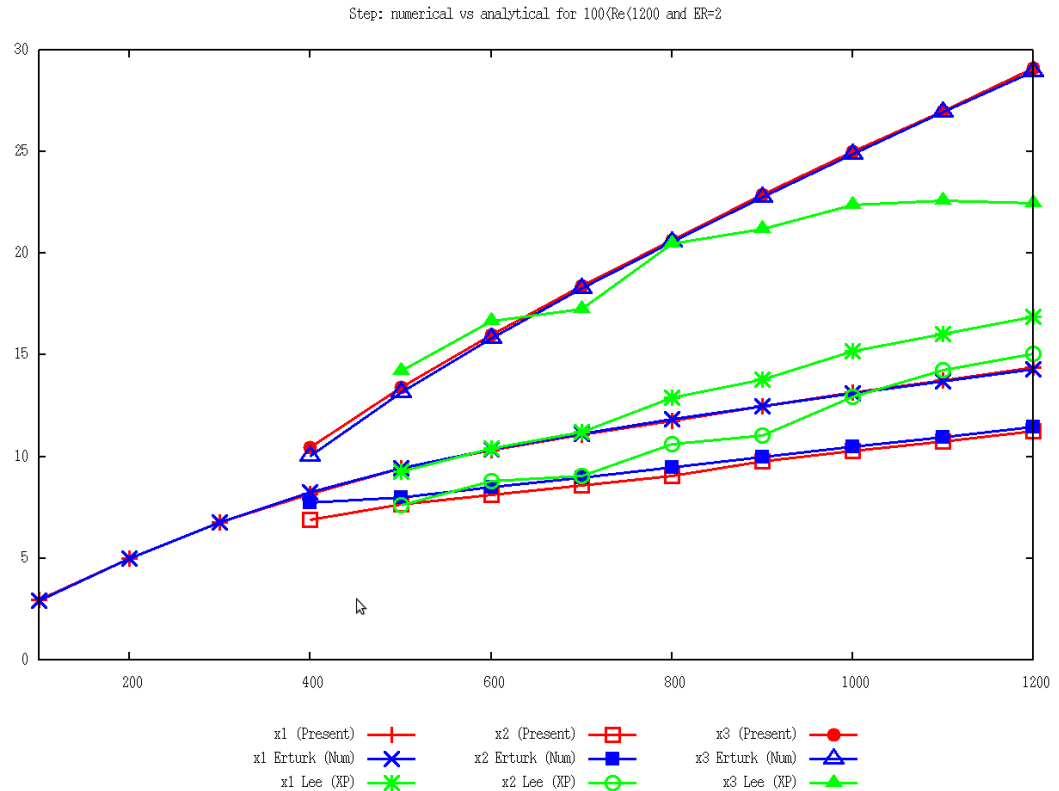
Figure 14 Comparison of x_1 (cross), x_2 (square) and x_3 (triangle) for ER=2 between present analysis (in Red) and reference numerical results (in Blue, see [10]) and reference experimental results (in Green, see [9]) for $100 \leq Re \leq 1200$

4- Wave Impacts and Slamming problems

4-1 Dam breaking

4-1-1 Model Description

Dam break waves have been responsible for numerous accidents making them a challenging field of research for numerical simulations. The Dam break test case is a classic validation problem for simulations involving free surfaces and consists in reproducing the collapse of a column of water under the influence of gravity and to study its propagation. Figure 15 a) offers a view of the mesh. The dimension and geometrical parameters are based on the experimental set up by [11].

4-1-2 Results

The results of Figure 15 b) show the propagation of the front with respect to time. Two different boundary conditions have been tested: free-slip and nonslip. The free-slip condition appears more diffusive than the non-slip condition. The non-slip boundary condition imposes a zero velocity in every direction while the free slip boundary only constrains the normal component. Consequently the free slip condition is more diffusive while the non-slip condition is closer to the reference experiment results by [11].
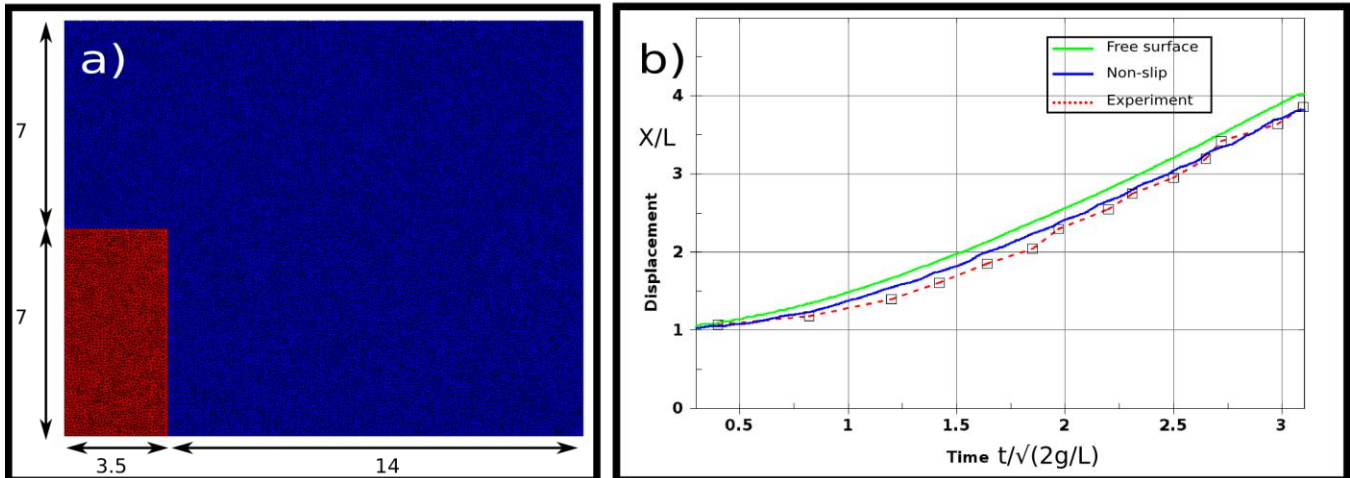
Figure 15 a) Mesh and Geometry used for the Dam Breaking test case b) Comparison between numerical results and reference experimental results by [11] for the Dam break test case.

4-2 Wedge-cone specimen impact on water

4-2-1 Model Description

This test case is based on the experimental results by [12]. Several hull bodies impacting the water at different prescribed constant speeds have been tested. The shape chosen here is that of a wedge cone specimen with its dimensions and shape described in [12]. The mesh size on the body will be of approximately $3 [mm]$. Results will be presented in terms of the slamming coefficient (non-dimensional force) defined in [12] as:

$$C_s = \frac{2\ F_{impact}}{\rho V_z^2 S_{max}}$$

where S_{max} is a reference are taken as the area of the orthographic projection of the impacting solid on the levelset surface ($S_{max} = 0.142\ m^2$ for the wedge-cone specimen), ρ is the density of the water and V_z the vertical impact force ($V_z = 10\ m.s^{-1}$ in this analysis).
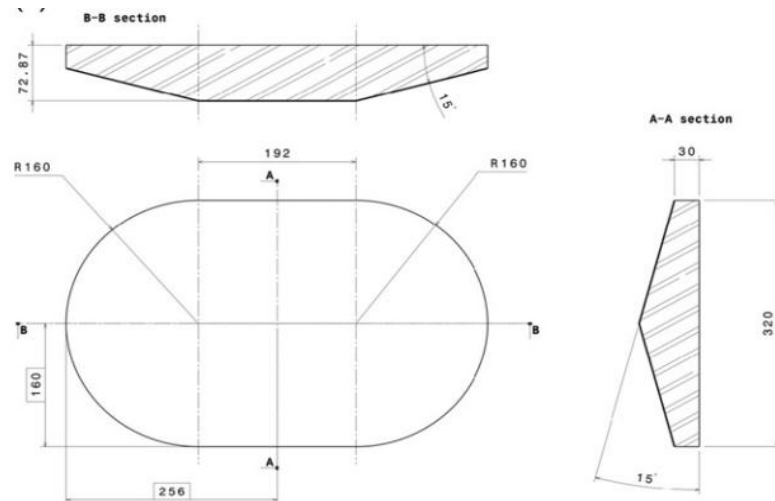
Figure 16 Geometry of the wedge-cone specimen. Sketch extracted from [12].

4-2-2 Results

As can be seen on Figure 17 and as in similar slamming cases, the sur-pressure that starts to appear at the impact instant "runs" along the wet surface as the body progressively enters the water. The sudden drop in the slamming coefficient happens when this sur-pressure reaches the end of the wedge. Using an implicit time step value close to the CFD condition, Figure 19 offers a comparison between a few points extracted from the reference experimental curves by [12] and the present numerical analysis. Although a slight overestimation of the peak value can be observed, the peak instant, the slope as well as the global behavior are correctly captured and the numerical results are therefore in good agreement with the reference experimental results.
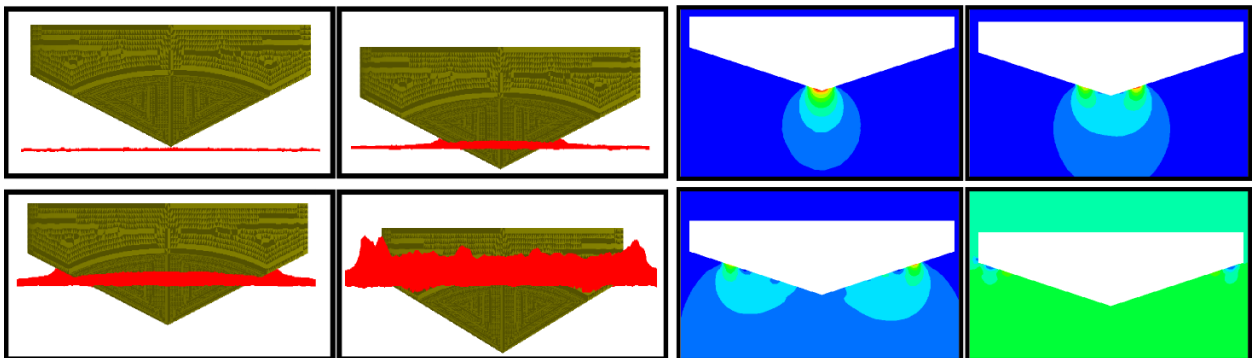

Figure 17 Visualization of the levelset surface behavior and pressure fringes as the wedge-cone enters the water in the A-A section plane.
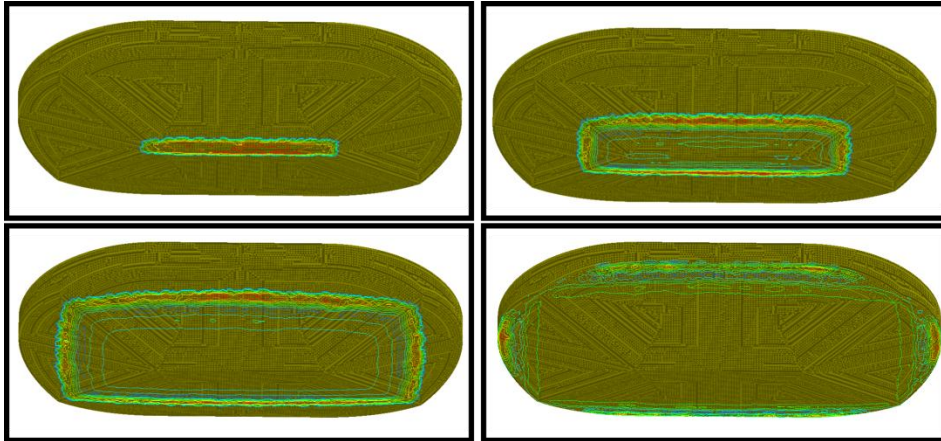
Figure 18 Pressure iso-contours along the bottom of the wedge-cone as it enters the water
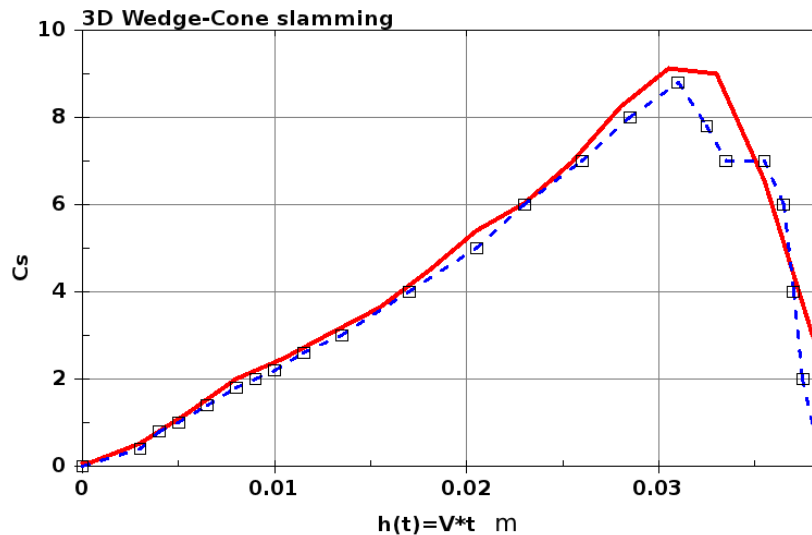

Figure 19 Comparison for the slamming coefficient between the current analysis (in Red) and some reference experimental points (in Blue) extracted from [12].

4-3 Free falling wedge impact on water

4-3-1 Model Description

For this slamming problem, a free falling wedge will be used. The wedge entering velocity is no longer prescribed and the wedge will slow down as it enters the water thus resulting in a fully coupled complex fluid structure interaction problem. The wedge is 0.5 m wide and 0.29 m high with a 30° dead-rise angle. The total length of the wedge is 1 m and will be treated here as a 2 dimensional problem. Figure 20 offers a view of the mesh used (surface element size along the wedge 0.001 m). The total weight of the wedge and the drop mechanism is 241 kg. An initial velocity of $6.15 \ m.s^{-1}$ is prescribed after which the wedge is falling freely. The vertical drop velocity will be compared to the results by [13].
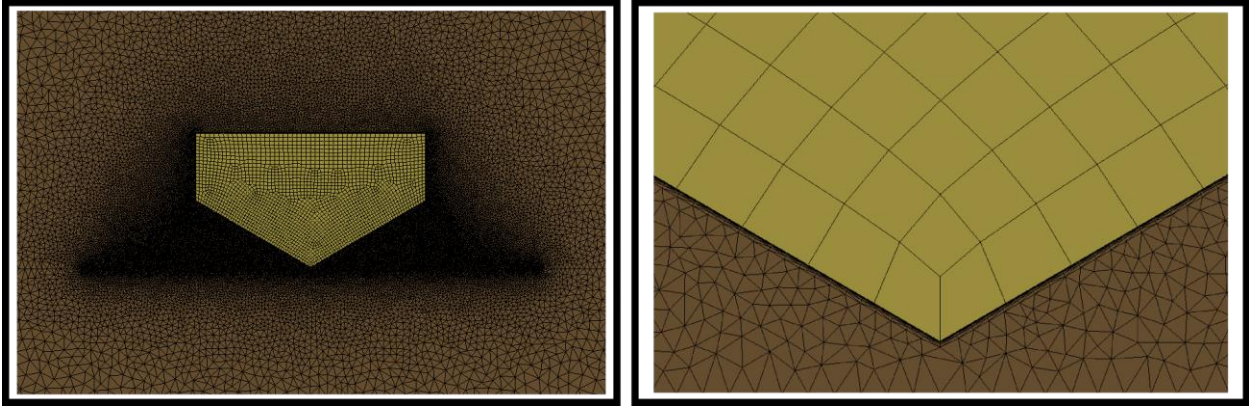
Figure 20 Various zoom levels on the free falling wedge case.

4-3-2 Results

Figure 21 a) shows the good agreement between the numerical analysis and the reference experimental results by [13] regarding the free fall velocity of the wedge. Figure 21 b) offers a comparison between the force extracted by simple derivation of the wedge velocity and the pressure drag force calculated by the ICFD solver further confirming the coherent fluid pressure repartition along the wedge.
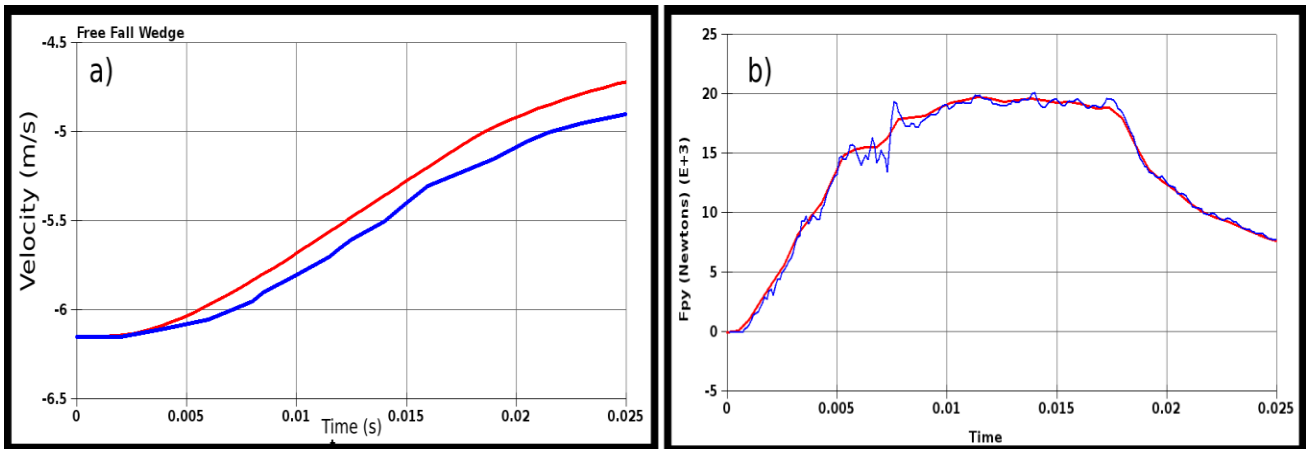

Figure 21 a) Comparison of the Vertical velocity of the free falling wedge between the numerical results (in Red) and the reference experimental results (in Blue) by [13].

5- Conclusion-Part 2

In the second part of this paper, several validation test cases have been presented. For each test case, some results have been extracted and compared to references. Additionally, some information on the mesh used was also given in order to give an approximate idea of the mesh size that is needed in order to get satisfactory results. These test cases have also been divided and organized in several domains in order to offer a clear view of the different potential applications of the ICFD solver. However, one must also bear in mind that future complex industrial analyzes may overlap several of these domains. For example, in the context of vehicle aerodynamic

design, the analysis of suspension systems integrated to the vehicle may be of interest. A set of springs and dumpers may be attached to the vehicle and the dynamic response of the suspension under the aerodynamic loads may be studied. This would result in a problem involving external aerodynamics and FSI. Some of the test cases presented here already combined FSI with Free surface. One could also imagine studying the sloshing phenomenon in a partially filled tank with liquid moving back and forth.

References

[1] S. Idelsohn, F. Del Pin, R. Rossi and E. Oñate, "Avoiding the instabilities caused by added mass effects in fluid structure interaction problems for pressure segregation and staggered approaches," *Int. Journal. Num. Meth. Eng.,* 2009.

[2] P. Jeongyoung, K. Kiyoung and C. Haecheon, "Numerical Solutions of Flow Past a Circular Cylinder at Reynolds Numbers up to 160," *KSME International Journal,* vol. 12, no. 6, pp. 1200-1205, 1998.

[3] A. Wolfgang, "Fluid Struktur Interaktion mit Stabilisierten Finiten Elementen," Universität Stuttgart Institut für Baustatik, Stuttgard, 1999.

[4] S. Ahmed, G. Ramm and G. Faltin, "Some Salient Features Of the Time-Averaged Ground Vehicle Wake," *SAE Technical paper Series,* 1984.

[5] B. J. and Al, "Using Cavitation technique to characterize the longitudinal vortices of a simplified road vehicle," Technical Report, PSA Peugeot Citroën, Drection de la recherche, , France, 2003.

[6] U. Ghia, K. Ghia and C. Shin, "High resolutions for incompressible using the Navier Stockes equations and a multigrid method.," *Computational Physics,* vol. 48, pp. 187-411, 1982.

[7] E. Erturk, "Discussion on Driven Cavity Flow," *International Journal for Numerical Methods in Fluids,* vol. 60, pp. 275-294, 2009.

[8] Cruchage and M. Oñate, "A Finite Element Formuation for Incompressible Flow Problems using a Generalized Streamline Operator," *Computer Methods in Applied Mechanics and Engineering,* vol. 143, pp. 49-67, 1997.

[9] T. Lee and D. Mateescu, "Experimental and Numerical Investigation of 2D backward facing flow.," *Computer and Fluids,* vol. 37, pp. 633-655, 2008.

[10] E. Erturk, «Numerical Solutions of 2D steady incompressible flow over a backward facing step, part i: High Reynolds number solutions.,» *International Journal for Numerical Methods in Fluids,* vol. 60, pp. 275-294, 2009.

[11] J. Martin and W. Moyce, "Part iv : an experimental study of the collapse of liquid columns on a rigid horizontal plane," Philosophical Transactions of the Royal Society of London, London, 1952.

[12] A. Tassin, A. Jacques, A. Alaoui, A. Neme et A. Leble, «Hydrodynamic loads during water impact of three dimensional solids : Modeling and Experiments.,» *Journal of Fluids and Structures,* vol. 28, pp. 211-231, 2012.

[13] R. Zhao, O. Faltinsen and J. Aarsnes, "Water entry of artibrary two dimensional sections with and without flow separation.," in *21st Symposium on Naval Hydrodynamics*, 1997.